In-situ measurements of energetic depth-limited wave loading

Pierre-Antoine Poncet, Benoit Liquet, Benoît Larroque, Frank d'Amico,
Damien Sous, Stéphane Abadie

In-situ measurements of energetic depth-limited wave loading

P.A. Poncet[a], B. Liquet[b,d], B. Larroque[a], D. D'Amico[a,c], D. Sous[a,e], S. Abadie[a]

[a]*Universite de Pau et des Pays de l'Adour, E2S UPPA, SIAME, EA4581, 64600, Anglet, France*
[b]*Universite de Pau et des Pays de l'Adour, E2S UPPA, LMAP - UMR CNRS 5142, 64013, Pau, France*
[c]*Universite de Pau et des Pays de l'Adour, E2S UPPA, LIUPPA, 64600, Anglet, France*
[d]*Department of Mathematics and Statistics, Macquarie University, Sydney, Australia*
[e]*MIO - Mediterranean Institute of Oceanography, Université de Toulon, La Garde, France*

Abstract

An extensive database of in situ measurements of wave impact pressure on the wall of a composite breakwater and associated explanatory variables (i.e., waves, wind, and water level) was collected in a particularly high-energy wave environment. Due to the bottom profile, which includes a wide mound of concrete blocks with a seaward edge that rises to the Lowest Astronomical Tide level over a large distance, most waves break before reaching the monitored barrier, making the data set representative of depth-limited wave loading. Maximum pressure is consistently found at the sensor position closest to the mean free surface, and statistically, a decrease of maximum pressure with the altitude is observed. Nevertheless, the database also shows a wide variety of vertical profiles of maximum pressure. A detailed analysis of the pressure signal shows that there are two impact classes associated with large pressure values. The first is mostly observed during stormy conditions with relatively slow pressure variations over time and a fairly uniform spatial distribution. The second class exhibits very limited pressure peaks in time and space and is most often observed during moderate sea states and high water levels. The pressure signals for each class agree well with the prediction of the PROVERB [35] impact classification based on breakwater dimensions,

---

water level, and wave parameters. Our dataset also shows the existence of impacts with simultaneous large pressure and rise time, which extends the range of the observed values of the pressure impulse already reported in-situ [10] from 31000Pa.s to 100000Pa.s. For strong impacts that show regular upward propagation, the peak pressure propagation velocity was estimated and most values remain below 20 m/s. Finally, we performed a statistical analysis to relate the maximum pressure to a number of variables, including offshore wave parameters, water level, and wind parameters. The multiple linear regression model created confirms the dominant influence of wave height and the negligible influence of the wind on pressure maxima. The other wave parameters are still significant but of secondary importance. Finally, the upper bound of the 99% prediction interval predicts the maximum pressure given a set of wave and water level conditions with a good confidence level which is an encouraging result.

1. Introduction

Understanding wave loading on coastal structures, in the broad sense (i.e., either artificial like breakwaters or natural like cliffs), is a necessary step to predict their stability. It remains a challenge owing to the complexity of the phenomenon which involves wave impact at the wave scale in a full three-dimensional environment.

Wave impact has been extensively studied since the beginning of the 20th century. Sainflou [41] and then Rouville et al. [40] first identified the existence of different types of impact. This typology mainly depends on the position of the breaking point with respect to the obstacle [25]. When the fictitious breaking point is located after the obstacle, the wave interacts with it as a sloshing flow, more and more violent as the breaking point gets closer to the obstacle. The critical case, in which the breaking point and obstacle share the same location, is called the flip-through impact [15]. The latter generates a very high-pressure peak in a short time. Sloshing and flip-through impacts mainly involve incompressible flows for which the pressure is well predicted by the theory developed in Wagner [49]. Compressible processes start to play a role as soon as air is involved in the phenomenon (i.e., when breaking starts just before the obstacle) either as small bubbles advected in the wave or as

a formed air pocket entrapped between the wave and the obstacle. Bullock et al. [12] categorized low and high aeration impacts. The first one occurs when the impacting wave contains relatively little air (typically less than 5%) and produces a high and short-duration pressure spike. In the second one, a well-defined cavity is entrapped, and the impact produces a short duration pressure peak followed by specific damped oscillations attributed to the variation of the air pocket volume. Bagnold [3] first proposed a model to account for this particular process. These phenomena have been studied extensively either numerically or experimentally in the last decades (e.g., [34, 36, 8, 43] among others).

This extensive knowledge is difficult to transpose to real situations owing to the complexity of the structures usually considered as well as of the surrounding environment itself. Seemingly, there are also differences in the wave impact process itself between laboratory and field conditions illustrated by maximum pressure value differences observed in both environments (i.e., 5600 kPa in controlled environment [8] and a little less than 800 kPa at full scale [11]). Peregrine [36] identified a few factors prone to damp maximum impact pressure in natural conditions compared to calibrate impacts in wave flume or numerical models. In particular, the three-dimensional effects inherent to real waves as well as the breakwater block armor units are likely to diminish impact pressure. Aeration processes, different in fresh and salted waters, and scaling in general make it also difficult to compare flume and field measurements [9, 7, 6, 37]. On the other hand, Peregrine [36] also mentioned that bathymetric wave focusing could conversely increase impact pressure in some particular cases.

The analysis of field data could help reduce the gap existing between the controlled and the natural environments [35]. Unfortunately, the amount of available data appears quite limited. One of the reasons for that is the difficulty to perform accurate and long-term measurements in such harsh conditions. Surprisingly, one of the most comprehensive data was obtained quite early in Rouville et al. [40] more than seven decades ago. Three piezo-resistive sensors, distributed vertically 1m apart, were installed on the slightly inclined wall of the Dieppe breakwater (northwest of France) around the mean water level (MWL) with a tide range of around 10 m. The bathymetry profile was composed of a pebble beach followed by masonry of slope 1:5 and finally the equipped wall. Rouville et al. [40] describes variable wave conditions including waves breaking directly on the wall trapping air. The maximal pressures recorded range from 180 to 690 kPa with breaking wave heights estimated

3

from 2 to 3.5m. Blackmore and Hewson [5] conducted in-situ wave impact measurements at the Ilfracombe seawall using seven pressure sensors over the vertical (from about 2 to 6 m). The waves were estimated visually at around 1m during the campaign which resulted in 112 impacts of less than 48 kPa. Although it is not indicated, according to the beach profile, the wave impacts measured should have been produced by broken waves. The few data obtained show linearly decreasing dynamic pressure with heights. More recently, Bullock et al. [10] carried out extensive wave impact measurements at the Alderney breakwater. They used a specifically designed sensor to record both pressure and aeration [4]. In that study, the maximal recorded pressure was 337 kPa at 6.2 m (Chart Datum) with weaker values at higher levels. Significant wave heights up to 3.1 m were reported. Bullock et al. [11] later obtained a maximal pressure of 745 kPa at the same site. The wave conditions which generated this value are not indicated. This paper also points out the lack of accessible field data for extreme conditions. Recent field measurements of wave impact have brought their interest to new site types. Cliff ground motion due to wave action was for instance conducted in Thompson et al. [48]. They showed that the dominant control on peak ground motion magnitude was wave impact type rather than the incident significant wave height, the larger ground motion being produced by wave breaking directly onto the cliff face compared to broken or unbroken wave impacts. Measurements of wave, current, and structure accelerations were conducted on La Jument offshore lighthouse under extreme wave conditions (a 19m high wave) in Filipot et al. [19].

While worth investigating, the link between field wave impact pressures and the expected explanatory variables, i.e. meteo-marine forcing conditions such as wave features and water level, appears significantly understudied in the literature. This is surprising as better knowledge in this direction could help improve the accuracy of the current empirical design formulas. Hence, for instance, Goda [20] and Takahashi [47] used to calculate the design load, a "design wave", assumed to be the largest wave in the design sea-state at the toe of the structure [21, 20, 35]. More specifically, these formulas require the design wave height, length and incident angle as input parameters among other ones (such as the geometrical parameters, etc.). In the field, the situation is more complex than in the laboratory, numerous interacting modes between the wave field, water level and the structure specificity can result in different pressure distributions on the structure. Regarding this aspect, the PROVERB project [35, 30], again, proposed a classification of impact

4

types depending on the breakwater dimensions, wave height and water-level illustrating this strong link. The water level influence on the breaking wave impact on vertical or quasi vertical walls is also stressed in Kirkgöz [27]. Wind may play a role in the phenomenon for instance by slightly shaping the wave [46] which may finally influence the local pressure field. Finally, Salvadori et al. [42] insists on the importance of the coupled influence of parameters on the critical load requiring a multivariate analysis to be relevant.

There are actually very few studies of broken wave loading as this condition is generally dismissed as not being very important. Nevertheless, although maximum pressures are known to be generated by waves breaking directly onto the structure, and especially in the case of low aeration impacts, broken wave loading should not be neglected, as they seem to produce a longer loading by increasing both the rise time and duration of the impact [12]. This feature may increase both the force and impulse on the structure [12].

In this paper, we propose high-frequency wave impact pressure measurements conducted at the Artha breakwater in Saint Jean de Luz Bay, south-west of France (See Larroque et al. [32] for a preliminary presentation of the experiment). Pressure data was collected in a wide range of forcing conditions, including very energetic wave conditions with significant wave heights up to 7.5 m. The data is now public and can be found in Abadie et al. [1]. Due to the particular bottom profile involving a wide mound of concrete blocks with a seaward crest that rises to the Lowest Astronomical Tide level over a large distance, most of the waves break before reaching the monitored obstacle and therefore the database is representative of depth-limited wave loading. In the present paper, input data such as significant wave height, significant period, mean swell direction, water level, wind speed and wind direction were simultaneously collected and added to the pressure data to form an extensive dataset suitable for statistical analysis. The objective of this statistical study is to better understand the role of the environmental variables on wave impact pressure in natural conditions. To our knowledge, this is the first time that this relation is investigated in the field.

In the first part of the article, the method employed for the measurements and the statistical models will be described. Then the results will be presented and finally, the discussion addresses several aspects of the problem.

2. Method

2.1. Presentation of the experiment

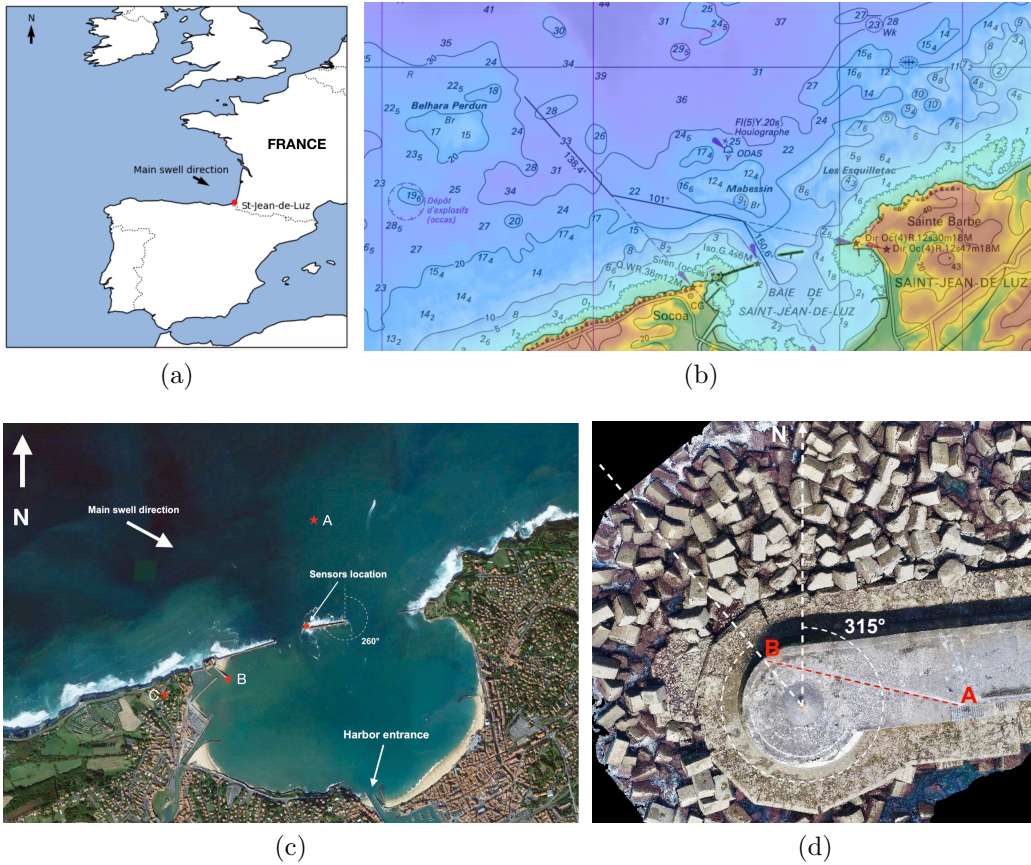#### 2.1.1. Configuration of the field site

(a)

(b)

(c)

(d)

Figure 1: Presentation of the study site with : a) Geographical position (red dot), b) Aerial view of the bay of St-Jean de Luz. The location of the sensors on the breakwater is indicated by a red dot. The red stars correspond to (A): The directional wave buoy, (B): Socoa tide gauge, (C): Socoa Semaphore. Source: Google earth V 7.3.2.5776. (2019/03/05). St-Jean-De-Luz, France. 43°23' 53"N, 1°40' 27"W, Eye alt 4 km. Maxar Technologies 2020, c) Bathymetry in the area of the Artha breakwater (depths in m - source SHOM website), d) Ortho-photograph of the Artha breakwater western roundhead. (A) : Acquisition station (B) Sensor location. The trench connecting the sensor to the acquisition station is visible along the red dashed line. The azimuth of the sensors to roundhead center axis is indicated. source: LP GEO 3D - Lycée Cantau / C. Bagieu.

6

The site considered for this study is the Artha breakwater in St-Jean de Luz, french basque coast, France (Figure 1 (a)). The Artha breakwater was built between 1872 and 1895 to protect the towns of St-Jean de Luz and Ciboure from flooding and erosion. Numerous concrete blocks were first immersed on an existing reef to create a high and stable bedrock. A large central caisson, made up of a mix of concrete and stones, surrounded by a concrete berm was then built on that foundation. The armour, made of more than 20000, 50 tonnes, cuboid, $4 \times 2.5 \times 2$ m^3 concrete blocks, defends the structure. The recurring displacement of blocks by the waves requires adding about 30 concrete elements every year. In addition to these maintenance operations, repairs of the masonry are also frequently required.

A directional wave buoy (Figure 1 (b) and (c)), part of the national CAN-DHIS network `http://candhis.cetmef.developpement-durable.gouv.fr/`, provides swell measurements 1 km offshore of the breakwater, in 20 m depth. The Socoa tide gauge is located within the bay of Saint Jean de Luz, less than 1 km from the pressure sensors. Socoa semaphore is 1km away and provides wind data.

The pressure sensors are located on the offshore facing side of the caisson, at the western roundhead (Figures 1 (c) and (d), and Figure 3) on the most exposed location. This position was determined based on observations of damages and climatology of swell parameters measured at the buoy.

The depth in front of the western round head is of 15m, but the bathymetry in the area is fairly complex with shallower areas on the eastern part and in front of Socoa breakwater (Figure 1 (b)). Several reefs and troughs can be identified which likely affect wave transformation from the offshore domain to the toe of the breakwater making refraction and shoaling processes complex in this area. Additionally, wave breaking more than 1km offshore is regularly observed during the strongest winter storms. In the bay, the depth is globally lower than 10 m.

2.1.2. Wave climate and tides

Kergadallan et al. [26] provides an overview of the statistical characteristics of the wave climate based on 7 years of measurements. The average climate is characterized by a percentile 50% of 1.26 m and 80% of 2.27 m for the spectral significant wave height H_{m0} (respectively 1.76 m and 2.93 m in winter) with an associated peak period T_p between 10 s and 12 s (respectively 11 s and 13 s). The 5-year return level of the significant wave height is 7.43 m (respectively 7.66 m and 7.85 m for the 10-year and 20-year values)

7

with 70% confidence interval between 7.09 m and 7.59 m based on a GPD fitting.

The peak direction of storm waves is predominantly from 315 °, with some events also reported from north-north-west. The tidal regime is mesotidal with 4.5 m spring tidal range around a mean water level of 2.64 m (C.D.).
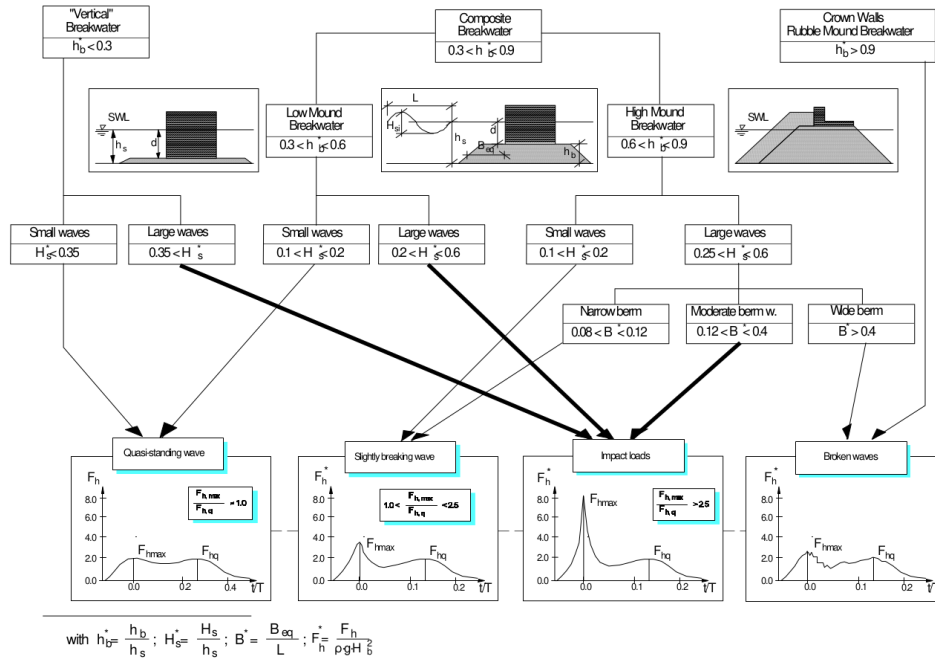
2.1.3. Load expected at the Artha breakwater

Figure 2: Typology of impacts in function of the breakwater type and geometry and waves and water level conditions. Source : PROVERB project chapter 2.2 [35]

The PROVERB classification (Figure 2) provides the shape of the load expected for a specific breakwater depending on three parameters : $h_b^* = h_b/h_s$, $H_s^* = H_{si}/h_s$, $B^* = B_{eq}/L_{pi}$, with h_s the depth at the toe of the breakwater, h_b the vertical distance from the toe to the berm, B_b the width of the berm, H_{si} and L_{pi} the wave height and length at depth h_s and $B_{eq} = B_b + h_b/2tan(\alpha)$.

To determine the category in the PROVERB classification to which the Artha breakwater belongs, the geometrical characteristics of the structure as well as the water level matter. Figure 3 shows two cross-sections of the Artha

8

breakwater. According to this, we may consider the averaged berm elevation as $h_b = 16.5$ m for the calculation. Then, considering the tide amplitude, h_s ranges approximately between 14.5 m and 19.5 m (Figure 3 (b)) leading to h_b^* varying from ≈ 0.85 for very high water levels to ≈ 1.13 for very low water levels. Therefore, for low to intermediate water levels, the Artha breakwater is considered as a crown wall rubble mound breakwater i.e., all the waves break before reaching the wall. In this situation, the load is likely to resemble the one depicted on the broken waves panel in Figure 2. At very high water levels, the breakwater should work as a composite breakwater and the load consequently depends on several other parameters. h_b^* being larger than 0.6, the breakwater is considered as a high mound breakwater. Small waves in the PROVERB classification (i.e., $H_s^* < 0.2$), which represent a maximum H_s of $\approx 3 - 4$ m, are supposed to generate slosh impact or slightly breaking wave impact as in the second panel of Figure 2. For larger waves, (say, $H_s > 5$ m) the relative berm B^* has to be calculated. Periods associated to such wave heights are expected to range between 15 and 17 s [?]. The calculation shows that the breakwater falls in the moderate berm category for which impulsive (impact loads in Figure 2) loads are likely to occur.

2.1.4. Sensors and acquisition station

To achieve high-frequency measurement in marine grade conditions, piezo-resistive sensors with a response frequency of 1 kHz and IP68 protection rating were selected.

A data acquisition station is installed on the protected side of the break-water, in a dedicated chamber [32]. It is connected to the sensors by a trench of more than 30 m, on the top of the roundhead, as seen in Figure 1 (d). The isolated nature of the site implies using a flexible and remotely programmable data acquisition system. To that end, a CompactRIO 9076 from National Instruments© was deployed with four NI-9203 modules (20 µA, 8 canals, 16 bits). With a 16 bit encoding, the digitization precision is suited to the accuracy of the sensors. The acquisition frequency of 10 kHz was selected with respect to the Shannon–Hartley theorem Shannon [44]. To download the data and modify the recording parameters if needed, a wireless system is used to communicate with the data acquisition station. To ensure the durability of the measurements, the installation is powered by a photovoltaic panel and a high-capacity battery with a solar charge controller. This setup allows measurements of wave impact over extended periods.
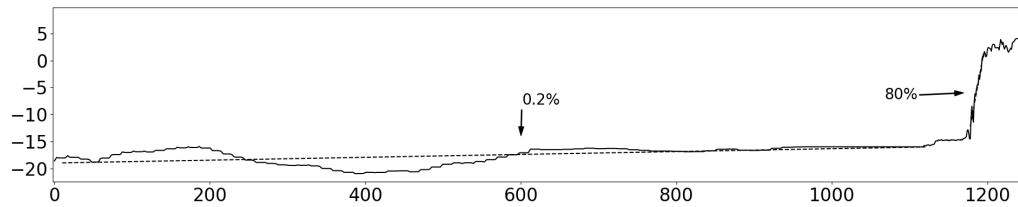
A preliminary campaign with two sensors vertically distant of 1.85 m was
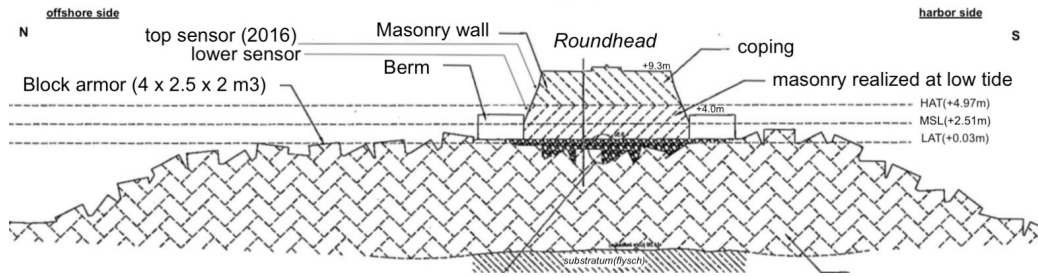
(a)
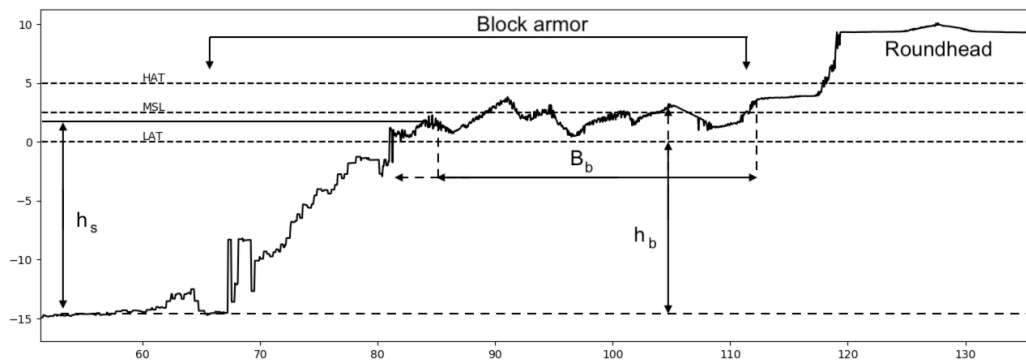
(b)

(c)

Figure 3: (a) Schematic cross section of the Artha breakwater roundhead perpendicular to the structure trunk. The main structural elements are mentioned as well as the position of the sensors during the 2016 campaign (b) Bottom level measured in a cross section of the Artha breakwater western roundhead along the axis passing by the lower sensor and the center of the roundhead. The equivalent PROVERB parameter are indicated. Altimetry is in chart-datum.(c) Bathymetric profile from the directional wave buoy to the Artha western roundhead wall. The two dotted lines are linear regressions of the two obvious distinct areas, namely, from the buoy to the structure toe and the block armor slope. The respective slopes of these regression lines are also indicated.

10

first performed in 2015-2016 [32]. In 2018, the installation was upgraded with 15 new sensors while the upper sensor of 2016 was removed. This provides a set of 16 sensors including the lower sensor of 2016. The two set-ups are presented in Figure 4. The highest water levels reach an area just above the sensor #0 and it is well known that the maximum impact pressure is more likely to occur around the water level. Therefore, a better placement of this new set-up would have been between the two older sensors. Unfortunately, this option was not accepted by the breakwater maintenance service who feared the embrittlement of the wall in this area (Figure 4 (b)). Because of this, the new set-up is not ideally placed vertically, and this is undoubtedly a limitation of our study.
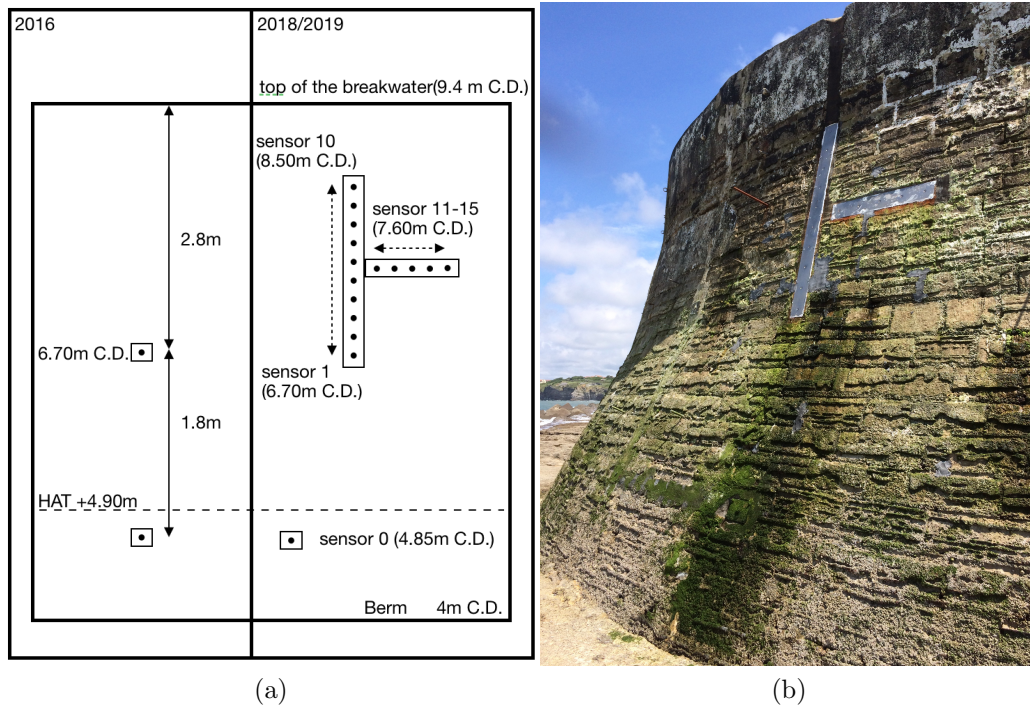

Figure 4: (a)Disposition of the sensors for both campaigns with the level of the berm, the level of the Highest Astronomical Tide (b) photograph of the installation (taken by the author)

11

2.2. Data overview

2.2.1. Environmental variables

The environmental parameters, whose measurement location is indicated in Figure 1 (b) are collected simultaneously with the impact pressures :

- 28 variables describing the sea state determined from 30 minutes observations, every hour, at the buoy A,

- w_l : water level as measured at B at the time of the burst, hourly,

- w_s and w_d : respectively mean wind speed and direction over 10 minutes as measured at C every hour,

2.2.2. Wave impact pressure data

The procedure of pressure acquisition and post-processing is described in detail in [18]. The acquisition station records wave impact pressure hourly in 10 minutes burst, with a sampling frequency $Fe = 10000$ Hz. An embedded threshold, just higher than the atmospheric pressure, allows saving only significant signals. With this threshold, approximately 300 to 400 bursts of 10 minutes are obtained every month. For each sensor, the maximal pressure observed over the 10 minutes burst provides an observation of P_{max}, our variable of interest or response variable. P_{max} is given after removing the offset due to atmospheric pressure.

The preliminary campaign carried out in 2015-2016 winter lasted four months, yielding 461 observations. In 2018-2019, the first successful tests were conducted in June and the main campaign extended from October 2018 to April 2019. A malfunction shut the station down between the 2018/12/07 and 2019/01/17, period during which, the waves conditions were mostly moderate. Overall, this second campaign resulted in 1390 observations.

The network of 16 sensors used during the campaign of 2018-2019 aims at giving an insight on the pressure spatial distribution. The spatial distribution is also used to evaluate the force by linear meter exerted on the wall. The calculation is made by integrating the instantaneous vertical distribution of pressure using a trapezoidal integration rule assuming pressure linearity between sensors. The linear profile is extended up to the top and down to the bottom to obtain the full force. Note that with the trapezoidal integration rule, sensor 0 has a major weight in the determination of the force as $z_1 - z_0 = 1.9$ m while the next $\Delta z = 0.2$ m, with z_i the altitude of the sensors. The bursts have been automatically processed by d'Amico et al. [18], 152999 impacts were identified overall in 2018-2019.

12

2.2.3. Rise time, pressure impulse, pressure peak propagation celerity and
force

Rise times and the impulse pressures statistics computed from the data of the 2018/2019 measurements campaign are also briefly analyzed in this paper. The rise time T_r is defined as the time between the beginning of the impact and the pressure peak for the highest pressure recorded in the burst. Pressure impulse, which corresponds to the time integral of the impulsive pressure peak is here approximated by $T_r \times P_{max}$. The pressure peak vertical celerity has been determined for the 2018-2019 dataset. The computation is limited to sensors 1-10, regularly spaced at 0.2 m intervals (sensor 0 was not considered due to its shifted location compared to the other sensors). Between two sensors, the celerity is calculated considering the peak pressure dates at each location and the distance between the two sensors.

Regarding the determination of the force from pressure measurements, Lamberti et al. [31] showed that the result is strongly dependent on the pressure sampling frequency and the distance between sensors. In order to obtain physical results, the sampling frequency has to be lower than the frequency corresponding to the inverse of the propagation time of the pressure peak between two sensors. Again, as sensor 0 is both horizontally and vertically, very distant from the rest of the array, the estimation of the force was performed only for sensors 1 to 10. Note that this computation can only be performed for impacts with a clear upward propagation of the pressure peak.

2.3. Statistical model

The relationship between the explanatory environmental variables and the response variable P_{max} is examined with multiple linear regression. At each timestamp i, the observation of P_{max} is expressed as a function of the ith explanatory variable observation plus a residual ϵ_i. The linear coefficients β_j associated with the explanatory variables are estimated using a least-squares method. By averaging the variable importance across all ordered combinations of variables, the so-called LMG metric [33, 22] determines the proportion of variability attributable to each variable. In parallel, the colinearity between variables has to be checked to ensure that it is low enough to be acceptable. For that purpose, the Variance Inflation Factor [39] is employed. A VIF below a threshold of 3 is usually accepted (see [13, 29, 23]).

3. Results

3.1. Data analysis

3.1.1. Environmental variables

The VIF analysis yielded the following 13 variables as noncolinear: the maximum period, the lowest measured free surface height, the maximum steepness, the period of the steepest wave, the skewness, the kurtosis, the correlation coefficient between successive wave heights, the spectral narrowness, the peak direction, the directional dispersion, the water level, the wind speed and direction. A multiple linear regression on this set of variables showed that only 4 variables among the 13 are significant, namely: the lowest free surface height, the maximum period, the peak direction, and the water level. One of the first results is therefore the negligible influence of the wind on the response variable (i.e., the maximum pressure over a time window). The 3 sea state variables can actually be replaced by $H_{1/3}$, $T_{H_{1/3}}$, and θ_m, more classically used for scaling purposes, without noticeably degrading the statistical model (adjusted R^2 of 54% instead of 58%), as they are strongly related to their counterpart.

Figure 5 presents the histogram of the latter explanatory variables for different thresholds of the response variable. The first column plots correspond to the distribution of the explanatory variables for all the impacts recorded by the station. As stated in [18], the embedded pressure threshold which triggers the data acquisition, is only slightly larger than the atmospheric pressure. These plots show how explanatory variables are almost normally distributed. Note that as the campaign duration is limited and due to the embedded threshold triggering the acquisition station, the data are therefore slightly filtered as evidenced by the water level plot. The second column shows the plots for a threshold of 10 kPa on the response variable; hence, the values of the explanatory variable favor moderate and strong impact pressures. Consequently, the smallest wave heights are less present. The wave incidence is in average slightly shifted to the north. The lowest periods disappear as well as the low water levels. Finally, in the last column plots, restricting the dataset to wave impact pressures larger than 100 kPa, wave heights are in majority in the range 3 -6 m, wave incidence is almost restricted to 0 −20 ° with a peak in 10 °, the period is comprised between 12 and 15 s, with a few events around 17 s or lower than 10 s and higher water levels are more frequent.

14

Regarding extreme events, the significant wave height measured at the buoy reached 7.5 m at 3 a.m. on 2016/02/09, and a swell period of 19.5 s was measured on 2018/11/18 at 3 am. All $H_s > 6$ m in this dataset are from the same storm event, which occurred on 2016/02/09. In terms of water level, the peak 5.01 m was reached at 5 am on 2019/01/23.
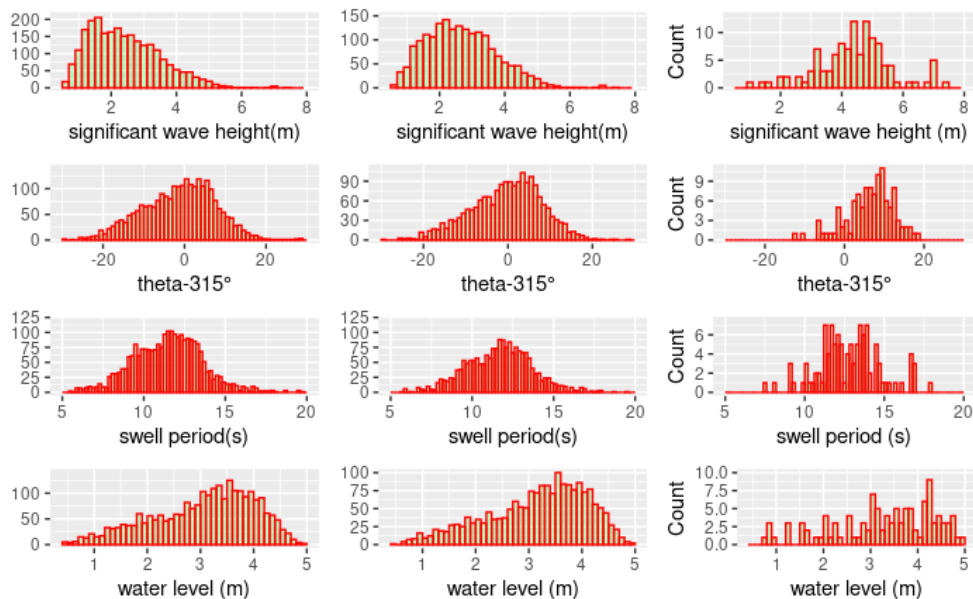

Figure 5: Histogram of the four explanatory variables ($H_{1/3}$, $T_{H_{1/3}}$, θ_m, wl) with different thresholds for the response variable : 0, 0.1 and 1 bar.

3.1.2. Maximal pressure and pressure impulse

The distribution of P_{max} at sensor #0 is presented in Figure 6 (a). The majority of impacts is below 100 kPa. Only 7 impacts are in the range 200 to 300 kPa. Among those 7 impacts, 4 happened during the same storm, in the night of the 2016/02/09. Only one of these P_{max} was recorded at the upper sensor #1 (see Figure 4 left), the 2016/02/09 at 4 am. The 2019/01/21 at 4 am an impact of 447 kPa was recorded at sensor #0 in moderate wave and wind conditions (i.e., $H_{1/3} = 1.5$ m, $TH_{1/3} = 8.2$ s, $ws = 4.6$ m/s, $wl = 4.39$ m). This is our maximum value so far.

The vertical distribution of P_{max}, restricted to large pressure values, is shown in Figure 7. Overall, there is a tendency of decreasing pressure values when moving up the wall. This is true for all the components of the boxplot,
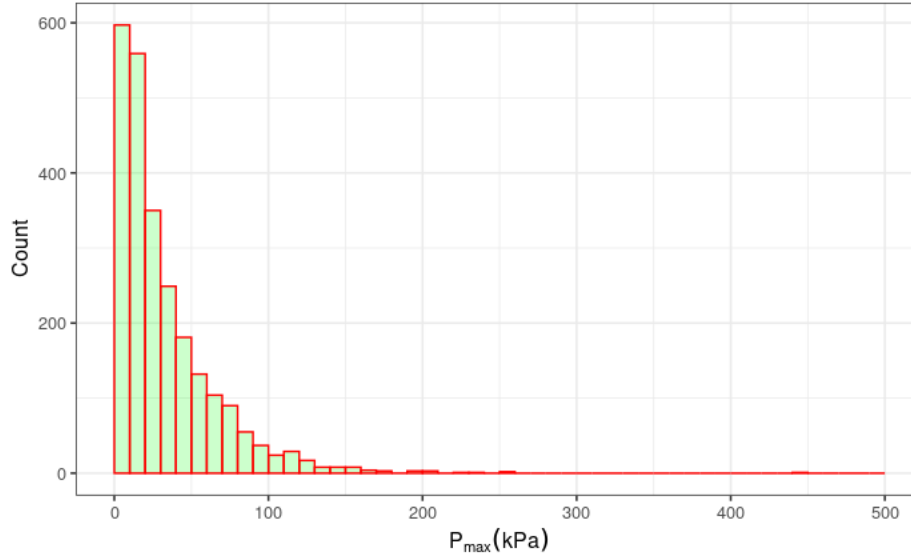
15

Figure 6: Histogram of P_{max} based on the observations over the whole measurement duration at sensor #0

namely the median value, the first and third quartiles, as well as the outliers. As a matter of consequence, extreme pressure values, larger than 200 kPa, only appear at the lowest sensor position.

Examples of pressure time signals are presented in Figure 8. The 2016/02/09 (Figure 8 (a,c,e)) was a particularly energetic storm with significant wave heights up to 7.5 m, water level up to 4.6 m and wind speed up to 21 m/s. On the other hand, the 2016/03/11 (Figure 8 (b,d,f)), a significant wave heights of 2.1 m, a water-level of 4.8 m and wind speed of 1.6 m/s were recorded. These cases illustrate two recurrent signal patterns observed in this experiment. In (c), many strong impacts can be observed in groups, while in (d), only one major impact is recorded. In the zoom windows, Figures 8 (e) and (f), two types of impact can be distinguished. The five impacts in (e) have a similar pressure signature, with a relatively rapid rise followed by a slower decrease, a stabilization at a relatively high value before going back to zero. In (f), a very sharp peak with a very rapid rise and fall is followed by a low steady pressure value before going back to zero.

To compare the different impacts, the ratio of pressure peak to quasi-steady level is used. This ratio was determined for 81 impacts of more than 100 kPa from the 2016 database. Most impacts are similar to the one pre-
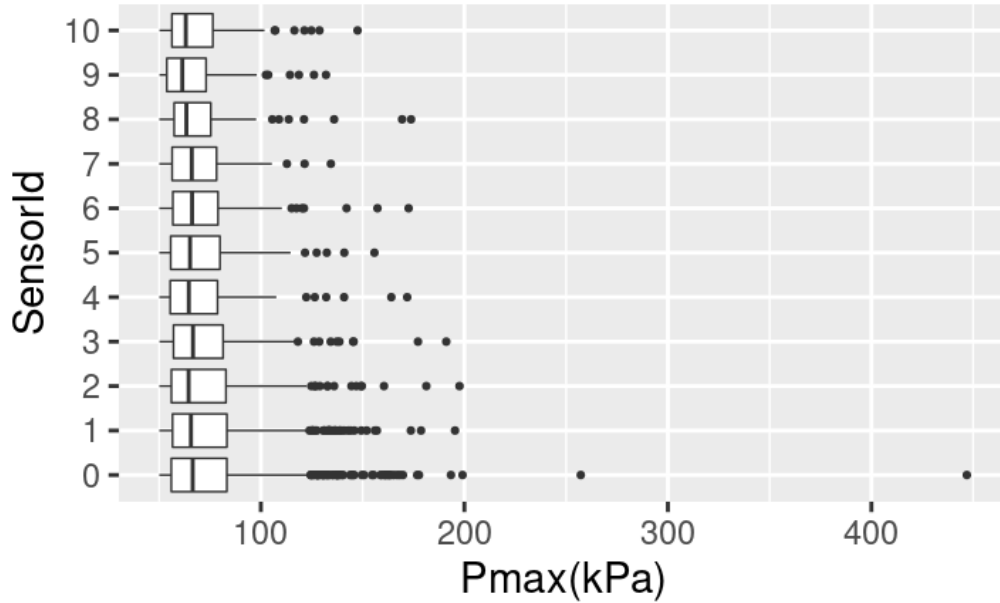
16

Figure 7: Vertical distribution of P_{max} represented as boxplots. Only impacts larger than 50 kPa are considered in this plot. Dataset restricted to the 2018-2019 campaign.

sented in Figure 8(c), and the mean ratio is 1.66 with a standard deviation of 26%. Among these 81 impacts, 8 presented a shape similar to (d). For these impacts, the mean ratio is 10 with a 3.5% standard deviation. They all present oscillations following the impulsive pressure peak with a main frequency around 15 to 20 Hz.

The vertical distribution of pressure impulse is shown in Figure 9. As for the maximum pressure, a decrease tendency of the magnitude with the sensor altitude is observed for the quartiles and the outliers.

3.1.3. Notable outliers

Among all the recorded impacts, the impact shown in Figure 10 is particularly interesting because of its magnitude and the presence of very well-defined, damped oscillations. This type of pressure signal is typical of a highly aerated impact, the oscillations likely being due to the compression and dilatation of a trapped air pocket. This impact, which occurred under moderate wave conditions (i.e., $H_{1/3} = 1.5$ m, $T_{H_{1/3}} = 8.2$ s), generated a very large impulsive peak of $\frac{p}{\rho_w g H_{1/3}} \approx 30$. In the power density spectrum,
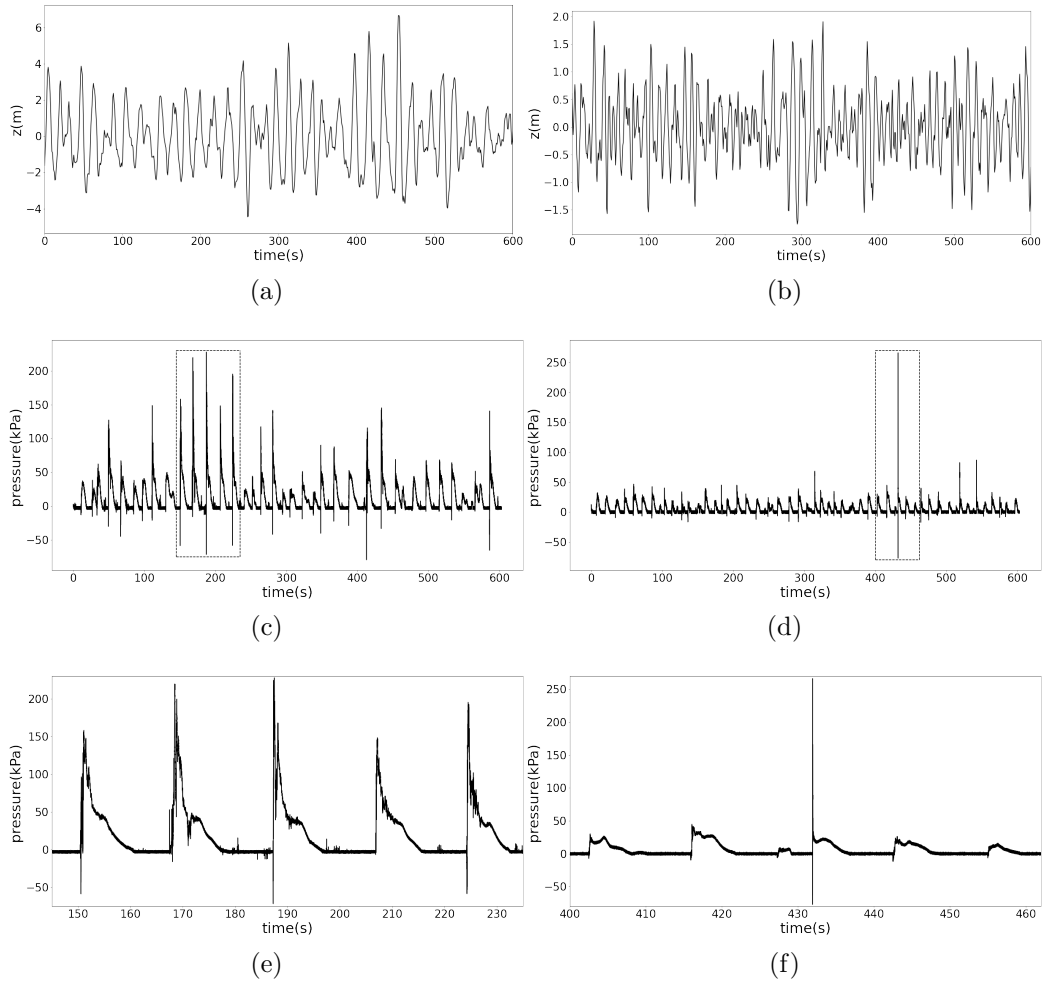
17

Figure 8: Examples of typical strong impact pressure time signals recorded at the Artha breakwater with the associated simultaneous free surface signal recorded at the buoy. Left column : 2016/02/09 at 4am, right column : 2016/03/11 at 5am. (a) and (b) free surface time signal recorded at the buoy location, (c) and (d) 10 minutes pressure burst at sensor #0, (e) and (f) Detailed signal within the dashed rectangles

shown Figure 10 lower panel, a well-defined peak at 29 Hz can be seen, so a little more than for the other impacts also involving pressure oscillations (i.e. between 15 and 20 Hz). In order to secure the interpretation of these oscillations, the plate holding the sensors was tested with an impact hammer and an accelerometer. The objective was to determine the natural frequencies of
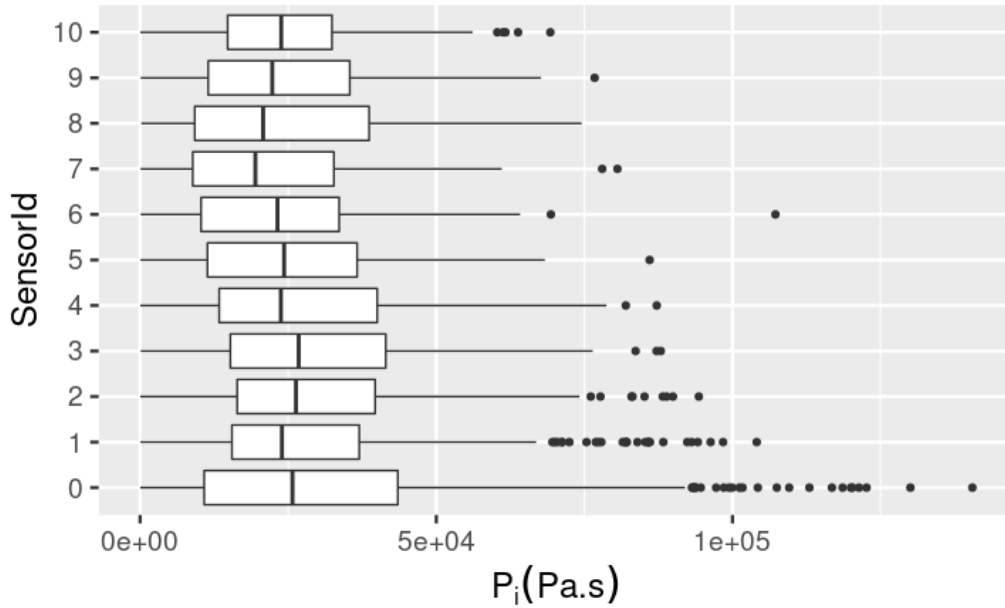
18

Figure 9: Vertical distribution of pressure impulse represented as boxplots. Only impacts larger than 50 kPa are considered in this plot. Dataset restricted to the 2018-2019 campaign.

the measuring system and compare them to the frequencies observed in these particular pressure signals. This test gave two non-negligible resonances of the measuring device at 470 Hz and 800 Hz, so at much higher frequencies than the one observed in those impacts. Therefore, the vibration of the plate is likely not responsible for the oscillation observed in the impact pressure.

3.1.4. Pressure peak vertical celerity and rise times

Impact measurements in-situ meet very different conditions leading to high variability. Regarding the pressure peak celerity along the wall, we tried to illustrate this variability by calculating the Spearman coefficients of the rank correlation between pressure peak dates and sensor elevations. The histogram presented in Figure 11 (a), for impacts greater than 50 kPa, shows the distribution of this Spearman coefficient. The perfect upward propagation is the highest bin, nevertheless, overall, the majority of the large impacts do not follow this expected upward propagation. A few rare events with an overall downward propagation are identified (negative Spearman value). It is suspected that many values in this histogram are representative of broken
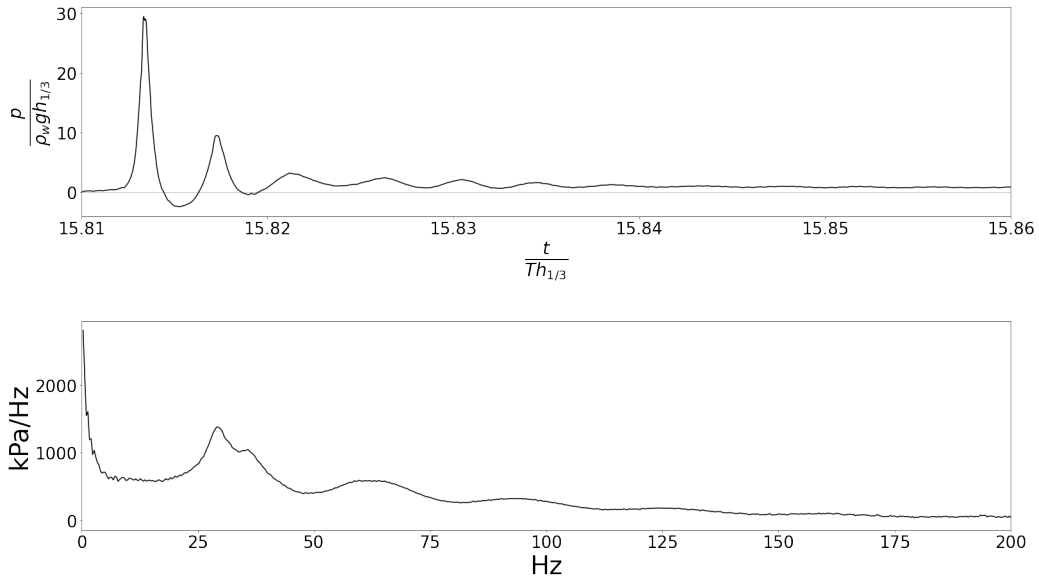
19

Figure 10: Top panel : dimensionless pressure history during the maximal impact of the 2019/01/21 4 am and associated power spectral density (bottom panel).

wave front hitting all sensors quasi-simultaneously, or random water projections from the block armor, rather than a well-defined upward propagation of a pressure spike.

Following this first analysis, the database was next restricted to impacts where the maximum index of sensors 1-5-6-8 (i.e., the most consistent of the array) was naturally sorted. The average velocity was then determined between sensors 1-6, since many impacts do not reach the threshold at the top of the array. This limited the database to 389 observations (38% of the database), most of which, involving a peak celerity smaller than 20 m/s (Figure 11 (b)). For example, the propagation velocity for the very impulsive impact presented (Figure 10) is ≈ 12 m/s.

In the lineage of Blackmore and Hewson [5], Bullock et al. [12], Cuomo et al. [16], Ariyarathne et al. [2], Kisacik et al. [28], Song et al. [45], Chuang et al. [14], the relationship between maximum pressure and rise time is shown in Figure 12. As expected, impacts with long rise time exhibit weaker pressure peaks while, on the contrary, impacts with a high value of P_{max} have a shorter rise time. In our observations, approximately 92.7% of the impacts are located under the contour $P_{max} = 31000/risetime$ which was the upper bound in [10]. A new curve, $P_{max} = 100000/risetime$, is introduced to better
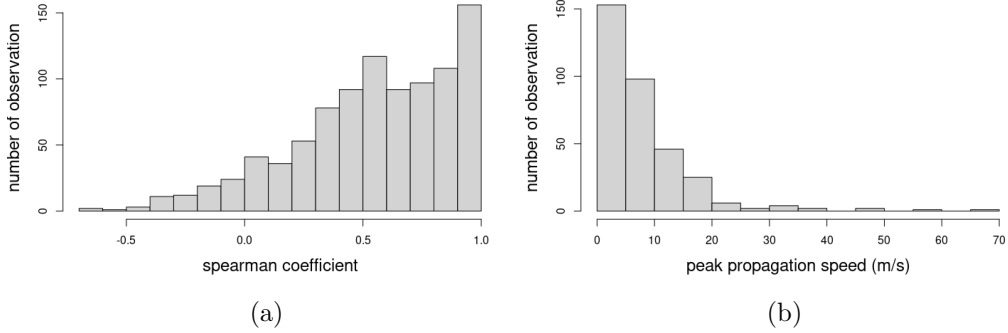
20

Figure 11: (a) Histogram of Spearman coefficients illustrating rank correlation between pressure peak dates and sensor elevations
(b) Histogram of pressure peak propagation vertical speed for impacts of more than 50 kPa calculated between sensors 1 and 6 with upward propagation only.

bound our data. This curve leads to a 0.1% exceedance rate. The dimensionless values are also presented in panel (b) using the same scaling as for instance, Kisacik et al. [28]
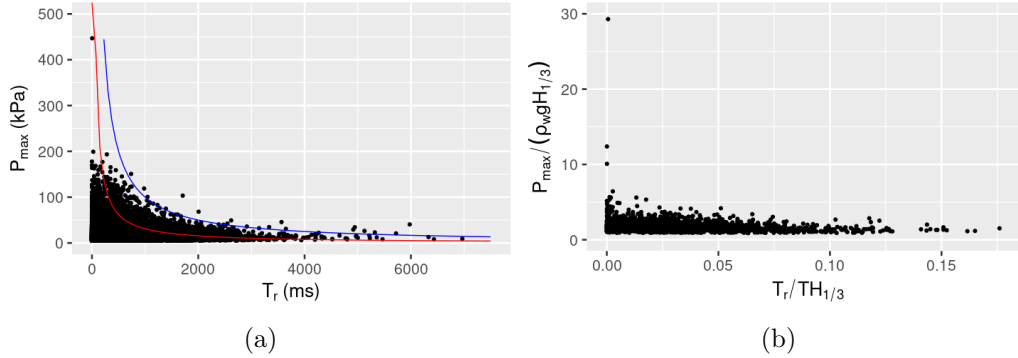

Figure 12: Relationship between maximal pressure and rise time for the 2018-2019 data. (a) In kPa and ms with the non exceedance curve of Bullock et al. [10] in red and the present 0.1% exceedance curve in blue, (b) Same as (a) but scaled.

3.1.5. Estimation of the force

An estimation of the force is presented in Figure 13 for the maximal impact of the 2019/ 01/23 at 06 am. As explained previously, to calculate

21

the force, the signal had to be downsampled to respect the condition given in [31], function of the pressure peak celerity. The pressure peak vertical propagation celerity is calculated as the slope of the regression line of the maximum pressure instant at each sensor in the t-z space. For this impact, the celerity is estimated at 8.3 m/s. This gives a quite low sampling frequency criterion of 40 Hz.

During this record, the significant wave height was 4.02 m and the water level 4.7 m. For this latter value, the water depth over the berm is only about 80 cm (Figure 2 (b)). Considering that the upper part of the block armor is almost at the same level as the berm over 30 m upstream , it is very likely that this impact was generated by a broken wave or a breaking wave at the latest stage. This curve therefore illustrates the pressure signal to be expected in this type of conditions. Compared to the classification presented Figure 2.1.3, it may be seen as an impulsive wave impact or an intermediate state between the impulsive impact and the broken wave impact. In our record, if the time scale appears coherent with Oumeraci et al. [35], the transition between the peak and the quasi-hydrostatic stage is smoother. The measured force maximum value (i.e., ≈ 0.7) should be interpreted with caution. Indeed, the pressure was only integrated over about one third of the wall. Multiplying by three this value would lead to something comparable to the values reported by Oumeraci et al. [35] for broken waves (i.e., around 2).

3.2. Statistical prediction of P_{max}

The preliminary analysis reported in section 3.1.1 already allowed to reduce the number of predictor variables to four. The database was also filtered to broken wave impacts in order to reduce the variability of the response variable. This is achieved by only considering water levels of less than 3.5 m or significant wave heights larger than 6 m. These conditions ensure that waves break before the wall and allow to remove the few events corresponding to waves breaking directly on the wall, which appear as outliers in the database. The database is then split into a training sample and a test sample (respectively, 80% and 20%). The multivariable linear model fitted to this sample yields an adjusted R^2 of 0.65. $H_{1/3}$ is the most important variable in the model and accounts for 73% of the explained variance, followed by θ_m, $T_{H_{1/3}}$, and water level w_l. The main interest of such a model is to provide a prediction of the maximum pressure expected for a given condition (i.e., an estimate of the maximum value among all the burst maximum pressures recorded for similar conditions). This is achieved with the 99% prediction
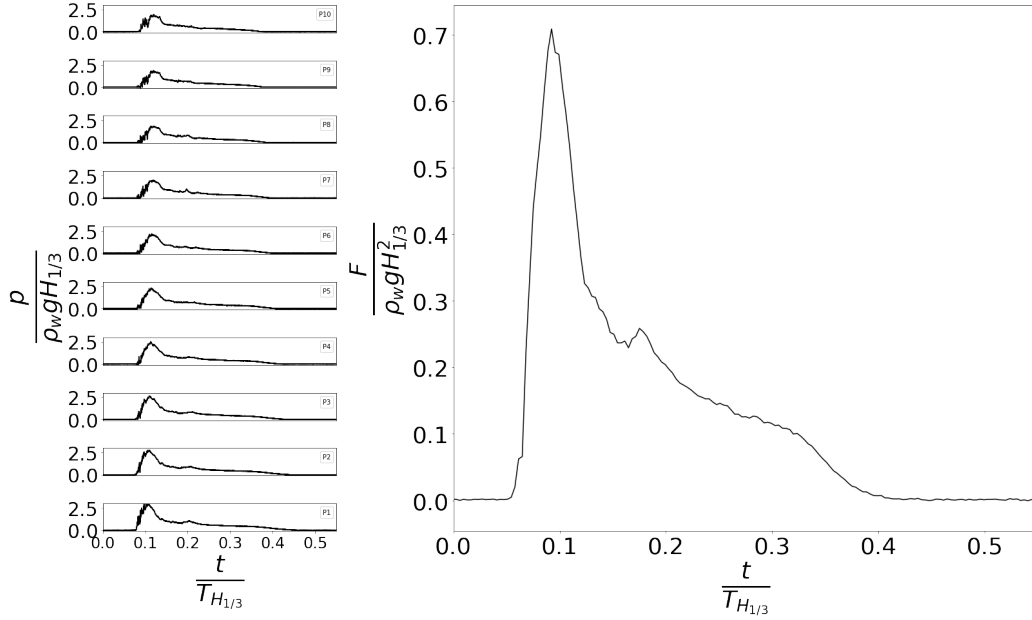
22

Figure 13: Pressure time history during the maximal impact of the 2019/01/23 6 am at each sensor on the vertical (left panel) and associated force signal sampled at 40 Hz following Lamberti et al. [31]

interval of the multiple linear regression model as illustrated in Figure 14. This figure illustrates the performance of the model in the plane $H_{1/3}$-P_{max}. For this test sample, the prediction is, overall, only exceeded by 3% of the subset observations.

The equation for the 99% prediction interval of the multiple linear regression model is given by :

$$P_{max_{99\%}} = \hat{P}_{max}(x_0) + t_{\alpha/2,n-p} \cdot s_e \sqrt{1 + x_0^\top \left(X^\top X\right)^{-1} x_0} \qquad (1)$$

With $\hat{P}_{max}$ the (mean) P_{max} predicted by the multiple linear regression, x_0 the vector of the predictors, X the design matrix, s_e the residual standard error and $t_{\alpha/2,n-p}$ the quantile of order $\alpha/2$ of a student distribution with $n - p$ degree of freedom (n number of observations, p number of predictor variables plus one).

23

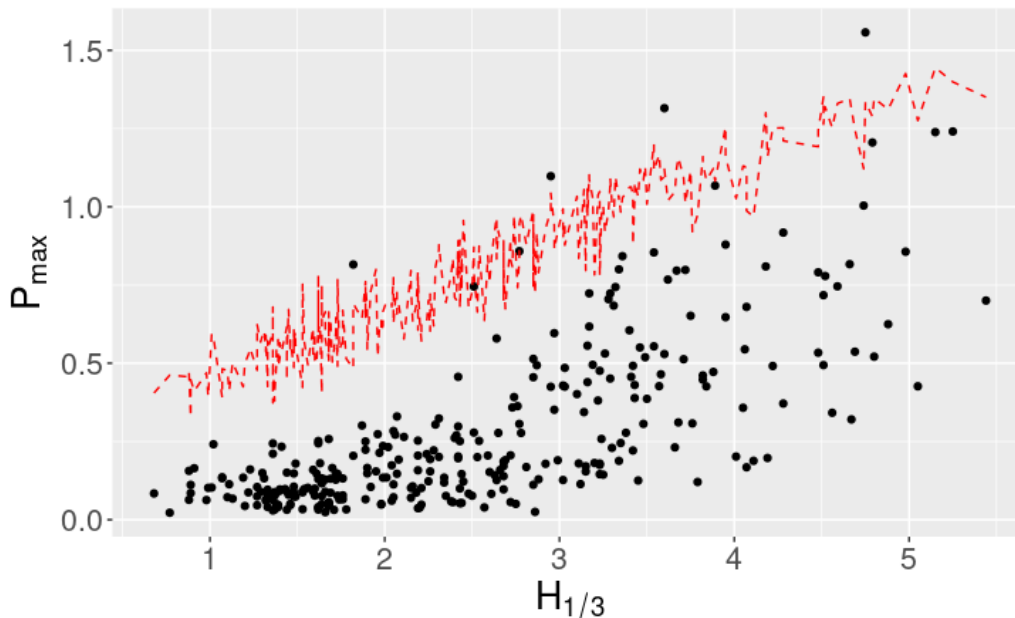Figure 14: Observation from the test sample and 99% prediction interval of the multiple linear regression model (dashed red line) in the $H_{1/3}$-P_{max} plane.

4. Discussion

All the studies reporting in-situ measurements of waves impacts have highlighted the difficulty associated with measurements in this harsh environment. Continuous very high-frequency measurements over a long period are challenging and therefore not frequent. As a result, most in-situ measurements were restricted to one or two years [5]. Overall very few in-situ data linking offshore wave conditions and impact pressure are available.

In the present experiment, two years of data have been collected so far but the particularly exposed nature of the site and the efficiency of the remote, independent station, allowing a quasi-continuous recording, has already provided a greater number of impacts than previous in-situ campaigns. Hence, 1851 10-minutes bursts at 10 kHz, reaching pressure of more than 10 kPa over atmospheric pressure have been collected, among which 122 included pressures of more than 100 kPa. During the 2018-2019 campaign alone, this makes more than 400 impacts of more than 100 kPa. This unique dataset offers the opportunity to provide wave impact statistics based on in-situ

measurements with a large number of observations. Moreover, these impacts were generated in wave conditions ranging from $H_s = 0.5$ m to 7.50 m so covering a wider range than in previous studies. The close proximity of a directional wave buoy, a tide gauge, and a semaphore additionally provide a relevant set of synchronised external variables to build a statistical model that relates the maximum impact pressure to the corresponding environmental conditions. To our knowledge, this is the first time such a model has been proposed based on field data. It should be noted that according to the bathymetric profile upstream of the breakwater and our observations and simulations [38], most of the waves impact the structure as broken waves, so this data set focuses particularly on this type of loading, which is rarely addressed.

The strongest impacts ($P_{max} \geq 200$ kPa) have been mainly observed in two types of conditions: (i) storm events with large significant wave heights or (ii) moderate wave heights and water levels of more than 4 m. In the second case(ii), the impacts present distinctive oscillations and a high impulsive peak to steady level ratio. The two classes are consistent with the classification proposed in Oumeraci et al. [35]. This classification predicts a behavior change of the Artha breakwater depending on the water level and the wave height.

Most of the impacts are generated by high waves. Figures 15 (a) and (b) shows a wave impact in this kind of conditions. As illustrated by this figure, it is reasonable to consider that they generally correspond to broken waves or waves at the latest stage of breaking as previously mentioned. Additionally, broken wave impacts are also predicted by the PROVERB classification [35].

According to [35], the impulsive impact type is likely to appear for very large water levels and moderate wave energy. An example of the condition favoring the occurrence of this type of impact is given in Figure 15 (c) and (d). Impacts belonging to this second class are not frequent and are likely to involve waves breaking directly on the wall. This type of impact is also characterized by very localized high magnitude short pressure peaks (Figure 13 (bottom left panel)) which may be the cause of the localized damages recurrently observed on the breakwater masonry. Our measurements show that these impacts are also associated with characteristic pressure oscillations which may be the signature of air entrapment [3, 12]. The observed frequencies around $20 - 30$ Hz are lower than those observed in, for example, Hattori et al. [24] with thin and thick entrapped air pocket, but closer to what was observed by Hofland et al. [25]. In Bagnold [3], the following expression is

(a)

(b)

(c)

(d)

Figure 15: Photographs of wave impacts at the sensor location with (a) and (b) : during a storm event on December 9 2019 around 4pm. $H_s = 5.9$ m, $T_p = 15$ s, $wl = 2.9$ m, courtesy of Bernard Bayle, and (c) and (d): in moderate wave condition and high water level (11/05/2018 1h45pm, $H_s = 2.70$ m, $T_s = 13.5$ s, $wl = 4.213$ m).

proposed to estimate the frequency of oscillation of the air pocket :

$$T_n = 2\pi \sqrt{\frac{\rho_w k_w D}{\gamma p0}} \qquad (2)$$

With D the thickness of the pocket, $\gamma = 1.4$ the ratio of the air specific heat at constant pressure to that at constant volume, k_w the thickness of the water mass effectively contributing to the impact and p_0, atmospheric pressure. Cuomo et al. [17] proposed the following assumptions to solve this equation in a realistic case: $D = \pi/12 \times H_{m0}$ and $k_w = 0.2(18\pi/12)H_{m0}$. Under these assumptions, the estimated period of oscillation of the air pocket would be $T_n = 6.4$ Hz for the impact of Figure 10. Therefore, the reduction in the oscillation frequency is probably mainly due to the larger scale involved in the present study.

As seen in Figure 8, sub-atmospheric pressure have been measured for numerous impacts, in two-part of the pressure signal. Either during the oscillation following the impulsive peak or just before the rise of pressure at the very beginning of the impact. The latter is also reported in Hattori et al. [24] who invokes the very fast upward motion of water at impact as a possible explanation.

Thanks to the pressure sensor array, wave impact pressure distribution is known and its statistical distribution, as well as specific impacts distribution, was studied. Overall the lower sensor is always the closest to water level and the box plots presented in Figure 6 shows an overall decreasing pressures from the bottom sensor to the top. This is in agreement with previous studies, including Goda [20], Cuomo et al. [16], showing that maximal pressure is located around the mean water level.

As previously indicated, the estimated force applied on the structure is consistent with the value proposed by the PROVERB classification with the scaled $F_{hmax} \approx 2$. The quasi-static part is weaker than the one predicted Figure 2.1.3. This might be due to an integration spatial domain of the force located significantly above the water level.

It is likely that large and long-lasting forces are required to cause potentially large displacements of structural elements. Here we show that these conditions correspond to those of a storm with large waves.

Figure 12 also shows that we have already recorded the largest pressure impulses in-situ reported in the literature. These events are represented by the points beyond the $31000/rt$ line and required the introduction of a new

0.1% exceedance curve defined by $100000/rt$. A good agreement is found with the laboratory experiments of Chuang et al. [14] and Kisacik et al. [28] using the same scaling as the latter reference.

For the events studied in this paper, involving mainly broken or wave being breaking (i;e., in a late stage of breaking), the multiple linear model built on the data show that the pressure maximum is mostly explained by the significant wave height. The other parameters of importance are, by decreasing order : direction, wave period and water level. Note that this order depends on the model used as a non linear GAM model fitted on the same data find the water level as the second parameter, behind the wave height [38]. Local wind speed and direction appeared not statistically significant . This is new result of the present paper, the wind effect being largely ignored in previous studies. In the preliminary statistical tests, very impulsive impacts appeared as outliers and were therefore removed to focus on broken waves. These impulsive impacts needs more observations to be better understood and may also require higher-level models such as machine learning algorithms to reach a possible prediction. Finally, for broken waves, we show that it it possible to predict with a reasonable accuracy the maximum pressure expected given a set of wave parameters and a water level based on the equation of the upper bound of the 99% prediction interval. Of course, the coefficients which appear in this equation are expected to depend on the particular structure studied, limiting thereby its application. Nevertheless, the fact that the maximum pressure is predictable in function of in-situ conditions is already an encouraging result in itself.

Finally, there are a few limitations in this study. First, the position of the sensors, fixed by technical constraints, is a limitation in this study. The lowest sensor is always the one the closest to the mean water level and it indeed regularly detected the highest pressures which is coherent with the present knowledge about wave impact. Nevertheless, the strong gap between sensors #0 and #1 prevented from getting information on the pressure profile in this crucial area.

The remote nature of the installation makes it complicated to access the station in case of failures, in particular during the winter season. Some failure occurred and generated some discontinuities in the acquisition. Progressive improvements of the station are ongoing to avoid such failures. It is therefore expected that a much larger and more comprehensive dataset will be available in a near future and provide a unique opportunity to better understand this complex process in nature.

5. Conclusions

High-frequency wave impact pressure measurements have been carried out at the Artha breakwater in Saint Jean de Luz France in particularly energetic wave conditions (H_s up to 7.5 m). The maximal pressure over 10 minutes and its dependency on off-shore wave parameters, local wind speed and direction and water level was studied. The following conclusions can be drawn from this work which mostly concerns depth-limited wave loading:

- the largest recorded pressure values are found at the sensor position the closest to the mean free surface. Overall, statistically, the maximum pressure decrease with the altitude.

- the strong impacts involve mainly two classes of pressure signals, in accordance with the PROVERB classification:

    – the first one corresponding to storm broken waves exhibits moderate peak pressure and relatively large quasi-hydrostatic loading. Those waves generate large forces over variable duration,

    – the second one (estimated to 10% of the large impacts), occurring during mild wave conditions and large water levels, are impulsive impacts with very large localized peak pressure followed by characteristic oscillations and moderate quasi-hydrostatic loading

- The dataset shows the existence of impacts with simultaneous large pressure and rise time (i.e.,large pressure impulse) which extends the range of the observed values already reported to 100000 Pas.

- Pressure peak propagation celerity has been evaluated and shows a wide range of values and even directions (i.e., downward). In case of upward propagation for impacts of more than 50 kPa, most values remain below 20 m/s.

- The statistical study relating the maximal pressure to the environmental conditions, for broken waves, shows that the significant wave height has a dominant influence overall. The wind influence seems negligible. Finally, given a set of wave and water level conditions, the maximal pressure expected can be predicted with a good accuracy (3% error) using the multiple linear upper bound.

29

References

[1] Abadie, S., Larroque, B., , Poncet, P., and D'Amico, D. (2022). In-situ measurement of wave impact pressure on the wall of a detached composite breakwater. seanoe database. https://doi.org/10.17882/87396.

[2] Ariyarathne, K., Chang, K.-A., and Mercier, R. (2012). Green water impact pressure on a three-dimensional model structure. Experiments in Fluids, 53(6):1879–1894.

[3] Bagnold, R. (1939). Interim report on wave-pressure research. Journal of the Institution of Civil Engineers, 12(7):202–226.

[4] Bird, P., Crawford, A., Hewson, P., and Bullock, G. (1998). An instrument for field measurement of wave impact pressures and seawater aeration. Coastal engineering, 35(1-2):103–122.

[5] Blackmore, P. A. and Hewson, P. J. (1984). Experiments on full-scale wave impact pressures. Coastal Engineering, 8(4):331–346.

[6] Bredmose, H., Bullock, G., and Hogg, A. (2015). Violent breaking wave impacts. Part 3. Effects of scale and aeration. Journal of Fluid Mechanics, 765:82–113.

[7] Bredmose, H., Peregrine, D. H., and Bullock, G. N. (2009). Violent breaking wave impacts. Part 2: modelling the effect of air. Journal of Fluid Mechanics, 641:389.

[8] Brosset, L., Marhem, M., Lafeber, W., Bogaert, H., Carden, P., Maguire, J., et al. (2011). A mark iii panel subjected to a flip-through wave impact: results from the sloshel project. In The Twenty-first International Offshore and Polar Engineering Conference, page 13. International Society of Offshore and Polar Engineers.

[9] Bullock, G., Crawford, A., Hewson, P., Walkden, M., and Bird, P. (2001). The influence of air and scale on wave impact pressures. Coastal Engineering, 42(4):291–312.

[10] Bullock, G., Obhrai, C., Müller, G., Wolters, G., Peregrine, H., and Bredmose, H. (2004). Field and Laboratory Measurement of Wave Impacts. Coastal Structures 2003.

[11] Bullock, G., Obhrai, C., Müller, G., Wolters, G., Peregrine, H., and Bredmose, H. (2005). Characteristics and design implications of breaking wave impacts. In Coastal Engineering 2004: (In 4 Volumes), pages 3966–3978. World Scientific.

[12] Bullock, G., Obhrai, C., Peregrine, D., and Bredmose, H. (2007). Violent breaking wave impacts. Part 1: Results from large-scale regular wave tests on vertical and sloping walls. Coastal Engineering, 54(8):602–617.

[13] Cenfetelli, R. T. and Bassellier, G. (2009). Interpretation of formative measurement in information systems research. MIS quarterly, pages 689–707.

[14] Chuang, W.-L., Chang, K.-A., and Mercier, R. (2017). Impact pressure and void fraction due to plunging breaking wave impact on a 2d tlp structure. Experiments in Fluids, 58(6):1–17.

[15] Cooker, M. and Peregrine, D. (1991). Violent water motion at breaking-wave impact. In Coastal Engineering 1990, pages 164–176.

[16] Cuomo, G., Allsop, W., Bruce, T., and Pearson, J. (2010a). Breaking wave loads at vertical seawalls and breakwaters. Coastal Engineering, 57(4):424–439.

[17] Cuomo, G., Allsop, W., and Takahashi, S. (2010b). Scaling wave impact pressures on vertical walls. Coastal Engineering - COAST ENG, 57:604–609.

[18] d'Amico, D., Larroque, B., Luthon, F., Poncet, P.-A., and Abadie, S. (2020). Continuous Measurement and Automatic Processing of In-situ Wave Impact Pressure Data. Journal of Coastal Research, 95(sp1):214 – 219.

[19] Filipot, J.-F., Guimaraes, P., Leckler, F., Hortsmann, J., Carrasco, R., Leroy, E., Fady, N., Accensi, M., Prevosto, M., Duarte, R., et al. (2019). La jument lighthouse: a real-scale laboratory for the study of giant waves and their loading on marine structures. Philosophical Transactions of the Royal Society A, 377(2155):20190008.

[20] Goda, Y. (1975). New wave pressure formulae for composite breakwaters. In Coastal Engineering 1974, pages 1702–1720.

[21] Goda, Y. (1988). On the Methodology of Selecting Design Wave Height, pages 899–913.

[22] Groemping, U. (2006). Relative importance for linear regression in r: The package relaimpo. Journal of Statistical Software, Articles, 17(1):1–27.

[23] Hair, J. F. (2011). Multivariate data analysis: An overview. International encyclopedia of statistical science, pages 904–907.

[24] Hattori, M., Arami, A., and Yui, T. (1994). Wave impact pressure on vertical walls under breaking waves of various types. Coastal Engineering, 22(1-2):79–114.

[25] Hofland, B., Kaminski, M., and Wolters, G. (2011). Large scale wave impact on a vertical wall. Coastal Engineering Proceedings, 1(32):15.

[26] Kergadallan, X., Le Berre, A., and Sanquer, R. (2021). Tome 1 - mer du nord, manche et atlantique - janvier 2021. Fiches synthétiques de mesure des états de mer du réseau CANDHIS.

[27] Kirkgöz, M. S. (1992). Influence of water depth on the breaking wave impact on vertical and sloping walls. Coastal engineering, 18(3-4):297–314.

[28] Kisacik, D., Troch, P., Van Bogaert, P., and Caspeele, R. (2014). Investigation of uplift impact forces on a vertical wall with an overhanging horizontal cantilever slab. Coastal engineering, 90:12–22.

[29] Kline, R. B. (2015). Principles and practice of structural equation modeling. Guilford publications.

[30] Kortenhaus, A. and Oumeraci, H. (1999). Classification of wave loading on monolithic coastal structures. In Coastal Engineering 1998, pages 867–880.

[31] Lamberti, A., Martinelli, L., Gaeta, M. G., Tirindelli, M., and Alderson, J. (2011). Experimental spatial correlation of wave loads on front decks. Journal of Hydraulic Research, 49(sup1):81–90.

[32] Larroque, B., Arnould, P., Luthon, F., Poncet, P.-A., Rahali, A., and Abadie, S. (2018). In-situ measurements of wave impact pressure on a composite breakwater: preliminary results. Journal of Coastal Research, pages 1086–1090.

[33] Lindeman RH, Merenda PF, G. R. (2006). Introduction to bivariate and multivariate. journal of statistical software.

[34] Lugni, C., Brocchini, M., and Faltinsen, O. M. (2006). Wave impact loads: The role of the flip-through. Physics of Fluids, 18(12):122101.

[35] Oumeraci, H., Kortenhaus, A., Allsop, W., de Groot, M., Crouch, R., Vrijling, H., and Voortman, H. (2001). Probabilistic design tools for vertical breakwaters. CRC Press.

[36] Peregrine, D. H. (2003). Water wave impact on walls. Annual Review of Fluid Mechanics, 35(1):23–43.

[37] Plumerault, L.-R., Astruc, D., and Maron, P. (2012). The influence of air on the impact of a plunging breaking wave on a vertical wall using a multifluid model. Coastal Engineering, 62:62–74.

[38] Poncet, P.-A. (2021). Characterization of wave impact loading on structures at full scale : field experiment, statistical analysis and 3D advanced numerical modeling. PhD thesis. Thèse de doctorat dirigée par Liquet, Benoit et Abadie, Stéphane Génie civil Pau 2021.

[39] Rawlings, J. O., Pantula, S. G., and Dickey, D. A. (2001). Applied regression analysis: a research tool. Springer Science & Business Media.

[40] Rouville, A. d., Besson, P., and Petry, P. (1938). Etat actuel des etudes internationales sur les efforts dus aux lames.

[41] Sainflou, G. (1928). Essai sur les digues maritimes verticales. Annales de ponts et chaussÈes, vol 98, tome II, 1928 (4) pp 5-48.

[42] Salvadori, G., Tomasicchio, G. R., and D'Alessandro, F. (2013). Multivariate approach to design coastal and off-shore structures. Journal of Coastal Research, 65(sp1):386 – 391.

[43] Scolan, Y.-M. (2010). Some aspects of the flip-through phenomenon: A numerical study based on the desingularized technique. Journal of Fluids and Structures, 26(6):918–953.

[44] Shannon, C. E. (1949). Communication in the presence of noise. Proceedings of the IRE, 37(1):10–21.

[45] Song, Y. K., Chang, K.-A., Ariyarathne, K., and Mercier, R. (2015). Surface velocity and impact pressure of green water flow on a fixed model structure in a large wave basin. Ocean Engineering, 104:40–51.

[46] Sous, D., Forsberg, P. L., TOUBOUL, J., and Nogueira, G. G. (2021). Laboratory experiments of surf zone dynamics under on-and offshore wind conditions. Coastal Engineering, page 103797.

[47] Takahashi, S. (2002). Design of vertical breakwaters. PHRI reference document nr. 34.

[48] Thompson, C. F., Young, A. P., and Dickson, M. E. (2019). Wave impacts on coastal cliffs: Do bigger waves drive greater ground motion? Earth Surface Processes and Landforms, 44(14):2849–2860.

[49] Wagner, H. (1932). Über stoß-und gleitvorgänge an der oberfläche von flüssigkeiten. ZAMM-Journal of Applied Mathematics and Mechanics/Zeitschrift für Angewandte Mathematik und Mechanik, 12(4):193–215.